Masters Thesis

Surface deformation due to slip on the San Andreas Fault as observed by InSAR

Mamta Sinha

Abstract

Satellite radar interferometric analysis of the ERS data reveals a wide-area distribution of creep along the San Andreas Fault towards north-west of a small town, Parkfield in California. This segment of the San Andreas fault is transitional in nature between the creeping segment of the fault to the the northwest and the locked Carrizo Plain segment to the southeast. The displacement due to the creep is measured across the fault and it distinctly shows the magnitude of the phase discontinuity decreasing from the northwest to the southeast. Another important observation is that the creep rate as deduced from the data is around 40 mm which is higher than the slip rate derived in literature, i.e. 25 mm. We use a single rectangular dislocation surface in an elastic half-space, after Okada, to model two contrasting fault slip-distribution at depth along the Parkfield segment. The first one assumes slip at all points on the creeping section and the second one has an area of no slip between the creeping parts. The surface displacements observed along the radar line of sight, from these models, show significant differences and the data matches the second model.

1   Introduction

Interferometric Synthetic Aperture Radar (InSAR) is a strong tool for creating high resolution topographic maps ([Zebker and Goldstein, 1986]) and measuring surface deformation over volcanoes ([Massonet et al., 1995]), areas

of ground movement due to earthquakes ([Massonet et al., 1993]) and glaciers ([Goldstein et al., 1993]). Two-pass and three-pass measurement data are used for differential interferometry to assess the deformation on the earth's surface. One of the most important advantages of InSAR is that it can accurately measure accumulated deformation over a period of time over a large area. In our study, we use InSAR images to detect and quantify the aseismic creep along the San Andreas Fault in Central California.

The Parkfield segment of the San Andreas Fault in central California has been the site of several moderate earthquakes at apparently regular intervals in recorded history of almost 150 years (Bakun and Lindh, 1985). Earthquakes of magnitude $M_w = 6.0$ shook the area in 1857, 1881, 1901, 1922, 1937 and 1966. This periodicity of approxiamtely 22 years led the seismologic community to predict another occurence of similar magnitude, no later than 1993. The absence of such an earthquake for the last 7 year has not deterred the scientists and Parkfield is one of the most monitored area for earthquake study. This is because Parkfield is the most likely place for an earthquake to occur in California.

The San Andreas fault is divided into several major sections. The Parkfield segment of the fault is a section of the North American-Pacific plate boundary. This fault segment is transitional between the central creeping segment of the San Andreas and a locked segment to the southeast of Parkfield. The transitional nature and the creep on the fault is observed by ERS interferometric measurements. Below depths of 10 to 20 km, the Pacific and North American plates have a uniform motion of 3.5 cm/year. The rate of fault creep measured at the Earth's surface on the other hand, decreases monotonically from 2.5 cm/year northwest of the fault segment to zero southeast of the Parkfield area, as described in literature, but we show otherwise.

Two contrasting kinematic models of the fault slip distribution at depth along the Parkfield segment have been described in the literature ([Harris and Segall], 1987). One model suggests that the northwest segment of the fault contains a 'stuck patch' at some depth, above and below which the fault is creeping. The other model has slip uniformly increasing from the surface till the value reaches the secular slip rate at seismogenic depths. We intend to show from our InSAR studies that the data more closely matches the 'stuck patch' model more than the other model.

2 Description of the Area and the Interferograms

2.1 The San Andreas Fault and Parkfield

The North American plate and the Pacific plate meet in western California, the boundary between them is the San Andreas Fault. It is a right-lateral slip fault, meaning that whichever side of the fault one stands, the other side will have a movement towards the right. The length of the fault is 1200 km, extending 550 km south of Parkfield and 650 km north of it. A simulated map of this area with the topographic contours and the San Andreas Fault and showing the location of Parkfield is in Figure 1.

2.2 Theory of InSAR

Synthetic Aperture Radar (SAR) systems record both amplitude and phase of the backscattered echoes. The phase of each pixel of a focused SAR image is the sum of three distinct contributions:

1. the two-ways travel path (sensor-target-sensor: hundreds of kilometeres in the satellite case) that, divided by the used wavelength (a few centimeters), corresponds to million of cycles;

2. the interaction between the incident e.m waves and the scatterers within the ground resolution cell;

3. the phase shift induced by the processing system used to focus the image.

Therefore, the phase of a single SAR image is of no practical use. But if two SAR images from slightly different viewing angles are considered (interferometric pair) their phase difference (interferometric frings) can be usefully exploited to generate Digital Elevation Maps (DEMs), to detect minute ground deformation and to monitor terrain changes.

The range changes can be calculated from the phase changes between the two images. It has been widely discussed and formulated by Zebker and Goldstein (1986), Rodriguez and Martin (1992), Prati and Rocca (2000) and others.
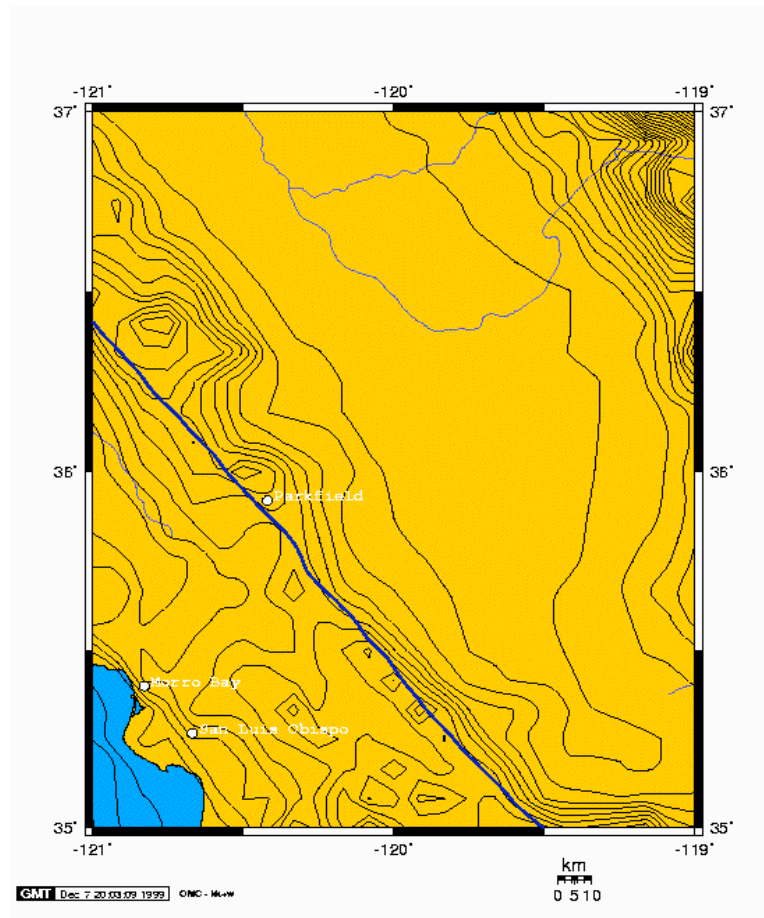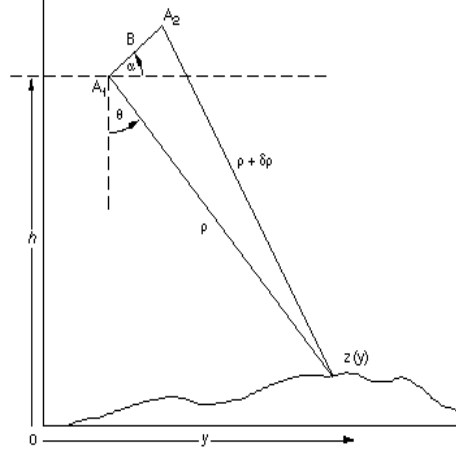
Figure 1: Map of the Parkfield area.

Figure 2: Basic imaging geometry for SAR interferometry. A1 and A2 represent two antennas viewing the same surface simultaneously, or a single antenna viewing the same surface on two separate passes.

As shown in Figure 2 , the two radar antenna A1 and A2 simultaneaously viewing the same surface, are separated by a baseline vector $\mathbf{B}$ with length B and angle α with respect to the horizontal. A1 is located at heigth h above some reference surface. The distance between A1 and the point on the ground being imaged is the range ρ, while $\rho + \delta\rho$ is the distance between A2 and the same point. The phase difference is sensitive to both viewing geometry and the height of the point z above the reference surface ($h = 0$) in Figure 2. If the viewing geometry is controlable or known to a sufficient accuracy, then the topography $z(y)$ or the displacement between two-passes can be inferred from the phase measurment to a precision of a few centimeters. The relevant equation to calculate range changes from phase difference measurments is :

$$\phi_{flat} = -\frac{4\pi}{\lambda} B_{perp} \frac{z}{\rho_0 sin\theta_0} + \frac{4\pi}{\lambda} \delta_\rho \qquad (1)$$

where ϕ_{flat} is the phase with the topography removed, λ is the wavelength, ρ_0 and θ_0 the slant range and look angle at the center of the scene respectively, and δ_ρ is the motion of the surface along the line of sight between data acquisitions (Rosen et al. 1996).

5

2.3   ERS Data Processing and Interferograms

The ERS data scenes for Parkfield were selected such that the combination of the interval between acquisitions and the baseline length would produce reasonable creep signatures. The scenes processed were all from frame 2889, track 256, with acquisition time interval varying from 9 to 15 months. The orbits include 10130, 25294, 5120, 12134 and 5621. A tandem pair of images acquired by orbits 24793 and 5120 with a baseline of 106 m was processed to get the DEM of that area. This DEM (in Figure 3) was subsequently used to remove topography from the deformation interferograms.

The amplitude image in Figure 3 clearly shows the surface signature of the San Andreas Fault oriented North-West to South-East. The interferometric pair which produced the best interferogram, as shown in Figure 4, was 10130 and 5120, with a time interval of 11 months and a perpendicular baseline of -36 m. The phase jump across the fault shows up as a sharp line coinciding with the fault on the amplitude image. The magnitude of the maximum phase differnce across the fault is of the order 2-3 radians, which translates to a deformation of approximately 9-13 mm, where a fringe or 2π radians correspond to 28 mm deformation along the radar line of sight. Two other interferograms quite clearly show the phase change signifying the creep along the fault. One of the first pairs processed was 10130-25294 with a perpendicular baseline of 2 m and a time interval of 10 months. Since the baseline was so small we did not need to do any topographic correction. It shows a distinct phase difference on the two sides of the fault. The signal and all the other information in the southern part is almost obliterated by a perpendicular noise signature which could be due to some atmospheric feature, maybe a cloud. Another interferogram with a reasonable phase difference across the fault was from the pair 12134-5621 (time interval = 15 months, bperp = 31 m). These two interferograms are shown in Figure 5.

The interferograms 10130-5120 and 12134-5621 had a significant baseline which contributed to a topographic factor in the images. This topography was removed by a DEM (Digital Elevation Map) made from a tandem pair 24793 and 5120. The DEM in Figure 3 successfully removed most of the topography from the above two interferograms.
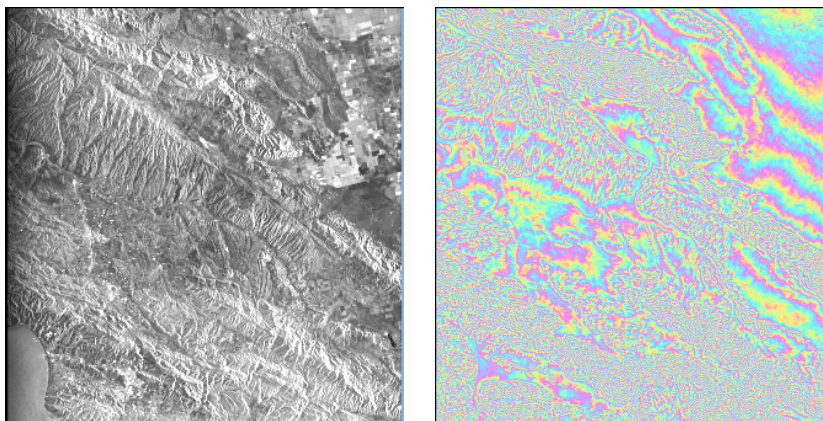
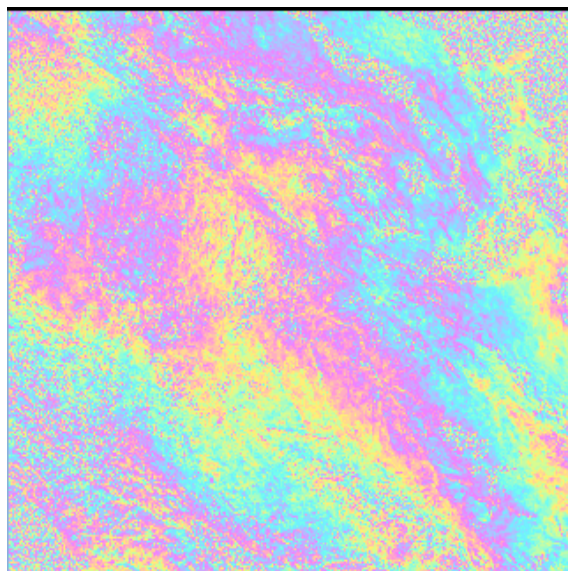Figure 3: *Left*, The amplitude image. *Right*, DEM to remove topography

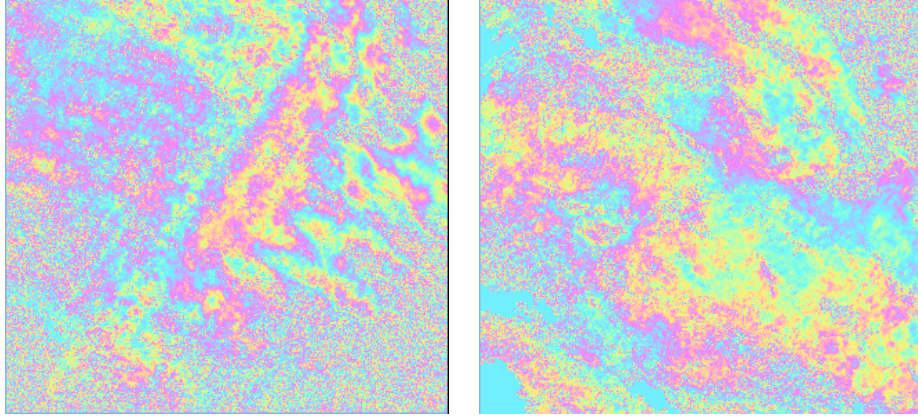Figure 4: Interferogram with the pairs 10130 and 5120.

Figure 5: *Left*, Interferogram with the pairs 25294 and 10130. There is an atmospheric signature across the fault. *Right*, Interferogram with the pairs 12134 and 5621

3   San Andreas Fault Slip Models

3.1   Theory

The deformation modeling was performed using a finite-source dislocation buried in an elastic half-space based upon the original work by Okada (Okada, 1985). There has been wide-range of studies on deformation of an isotropic homogeneous semi-infinite medium based on the dislocation theory. Okada presents a complete set of closed analytical expressions for the surface displacements due to inclined shear and tensile faults in a half-space for both point and finite rectangular sources. These expressions are particularly compact and free from field singular points. Elastic medium occupies the region of $z \leq 0$ and x axis is taken to be parallel to the strike direction of the fault. The elementary dislocations are U_1, U_2 and U_3 which correspond to strike-slip, dip-slip and tensile components of arbitrary dislocation. The dip angle is δ, the length of the fault is L, the width is given by W and the depth of the lower boundary of the fault is d. The rectangular dislocation is defined by ten parameters: length, height, strike, dip, and location (given by the three coordinates of the center of the dislocation, which accounts for three parameters) and the three parameters of displacement across the dislocation: dip-slip,

8

strike-slip and opening.

3.2 Approach and Comparisons

The area is taken to be a 100 km by 100 km grid where the fault passes approximately diagonally across it from the northwest to the southeast. The fault strikes N139°E. Since the San Andreas fault is a vertical fault, the dip is 90°. For all the models we constrain the dip-slip and the opening to be zero because the fault in consideration is assumed to have purely strike-slip. The slips on the fault have a negative value based on the convention for a right lateral slip. The slip values on the creeping section is assumed to be 40 mm per year. This is higher than the expected slip because as explained in the next section, this value matches the data better than the lower and expected value of 25 mm. In the locked section the slip is the same for all the models i.e. no slip till 15 km depth and 35 mm slip rate below it. The locked section slip profile is at the bottom right of Figure 6. Three different slip models are described in the following sections:

3.2.1 Model 1

This model is very simple and rather unrealistic, with a uniform slip of 40 mm/year on the creeping section till a depth of 15 km. Below 15 km, the slip rate equals the secular rate of the plate movement which is assumed to be 35 mm/year. The slip rate versus depth is at the top left of Figure 6.

3.2.2 Model 2

In this model everything remains the same except that the slip on the creeping section of the fault decreses linearly from 40 mm/year at the surface to 35 mm/year at a depth of 15 km below which the rate is 35 mm/year (top left of Figure 6).

3.2.3 Model 3

This model takes into consideration the 'stuck patch' on the creeping section. We assume the slip rate to be decreasing from 40 mm/year at the surface to 0 at a depth of 3 km. The locked zone is from 3 km to 8 km deep and then the slip increases from 0 to 35 mm/year at 15 km depth and stays at 35 mm/year below it. The slip rate profile is in the bottom left of Figure 6. Another similar

model is at the bottom center of Figure 6 where the locked patch extent is from 5 km to 10 km deep.

3.3   Deformations along the radar line of sight

The ERS satellite descending flight path is N9°E. The satellite looks down to the right, so the look angle is W9°N on the ground as shown in the left of Figure 7. The radar looks sideways at an angle of 23° to the vertical (right figure in Figure 7).
Thus, the radar line-of-sight vector is given by:

$$R = -(sin23cos9)i + (sin23sin9)j - (cos23)k; \tag{2}$$

To calculate the component of surface deformations in the direction of the radar line-of-sight, we calculate the dot-product of the deformation vectors with the radar line-of-sight vector:

$$u_R = u.R \tag{3}$$

Figures 8, 9, 10 and 11 show the deformation along the line of sight of the radar and the displacement profiles along the line AB across the fault, fault for Model 1, Model 2 and the two variations of Model 3, respectively.

3.4   Comparisons of the data with the models

In the interferogram 10130-5120, one section of the fault is dominantly visible but there is a hint of another smaller section to the left of the main, towards the center of the image. The phases across the main fault were plotted as scatterplots starting from the north-east corner of the fault in the image to a little beyond the point where the fault creep vanishes as one goes south-eastwards. The scatter plots in Figure 12 show the diminishing phase difference across the fault. The phase jumps from the above scatterplots, along with some more phase jump values across the main section of the fault is plotted in Figure 13 as the x's. Four phase jump values were also taken from the smaller section and plotted in the same figure as the dots. These phase jumps are at different locations along the fault, measured from its north-east corner in the image.
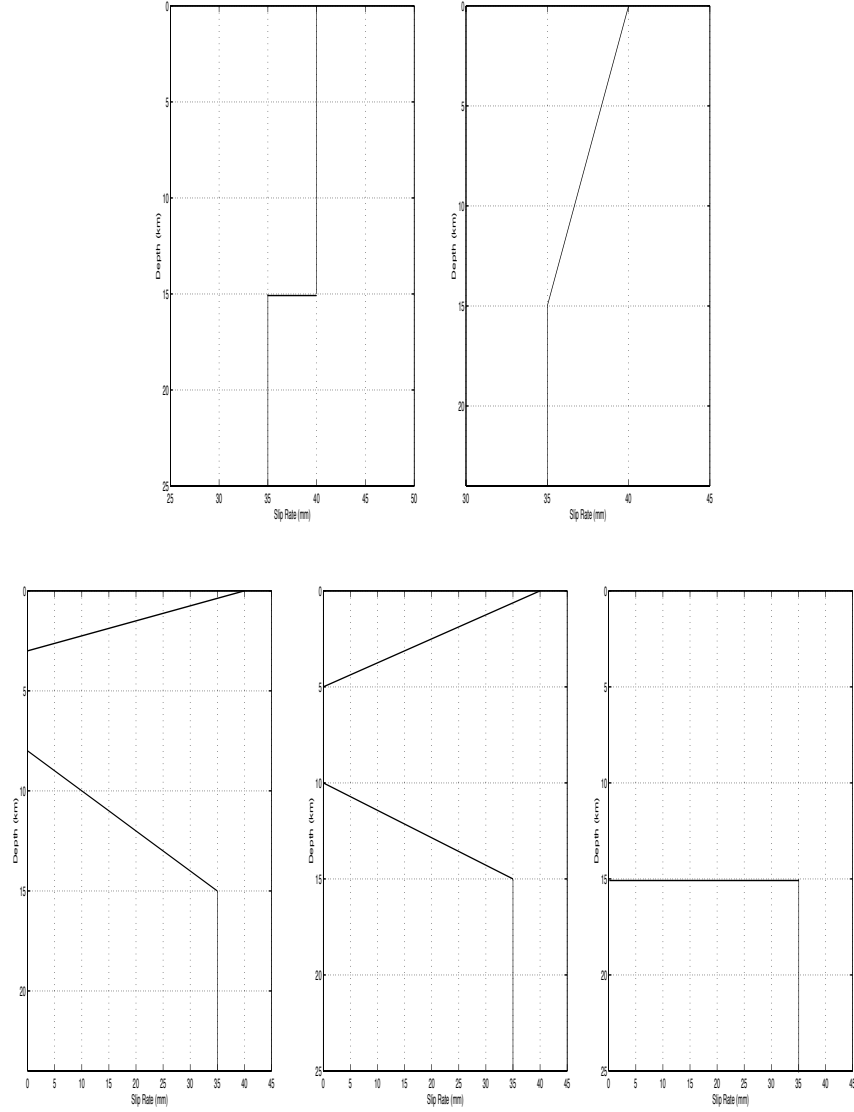
Figure 6: *Top Left*: Slip Profile for the creeping section of Model 1, *Top Right*: Slip Profile for the creeping section of Model 2, *Bottom Left*: Slip Profile for the creeping section of Model 3, with 'stuck patch' extent of 3-8 km, *Bottom Center*: Slip Profile for the creeping section of Model 3, with 'stuck patch' extent of 5-15 km, *Bottom Right*: Slip Profile for the locked section of all the models.
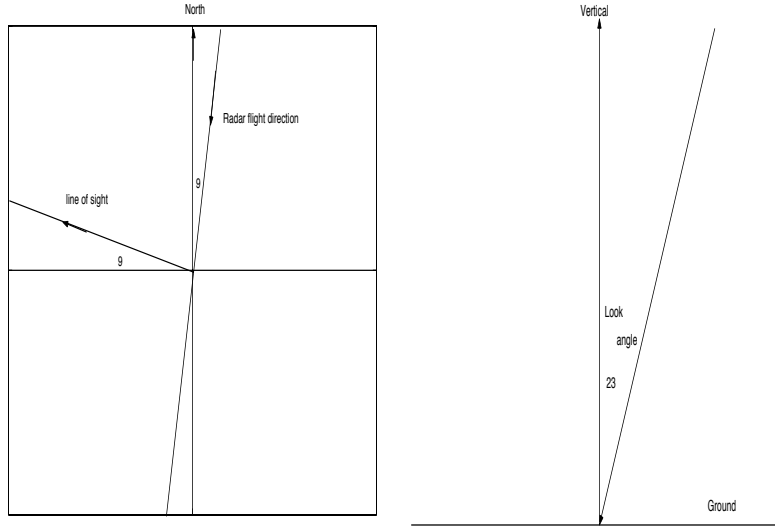
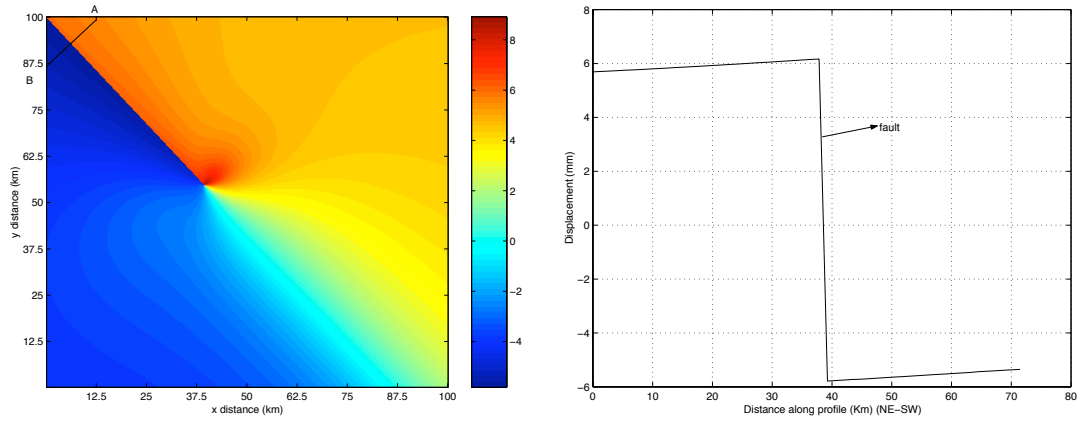Figure 7: *Left*: Radar line-of-sight and *right*: look angle

Figure 8: *Left*, Deformation along the radar line-of-sight for Model 1. *Right*, The profile along the line AB.
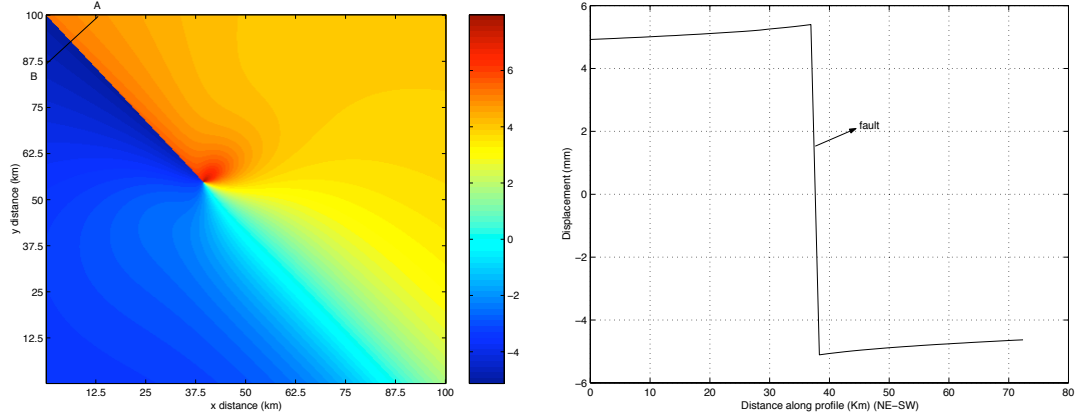
Figure 9: *Left*, Deformation along the radar line-of-sight for Model 2. *Right*, The displacement profile along line AB.
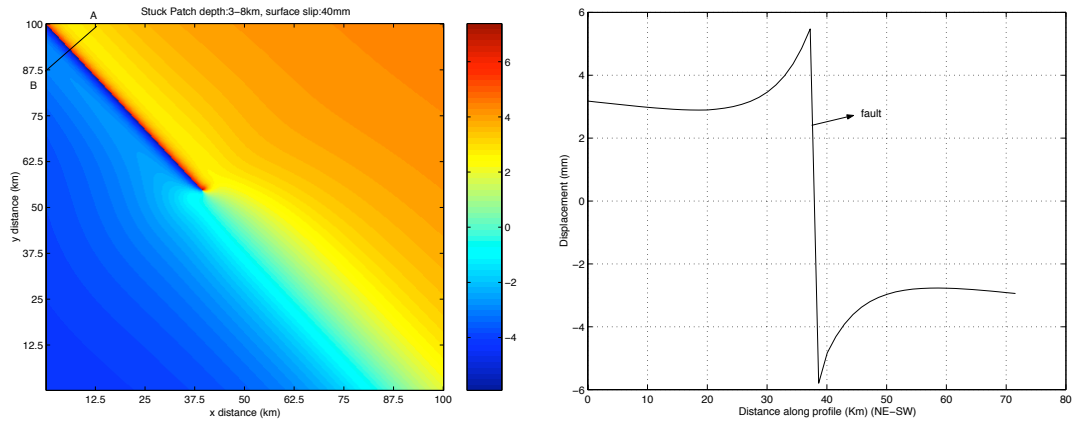

Figure 10: *Left*, Deformation along the radar line-of-sight for Model 3. *Right* Displacement profile along line AB
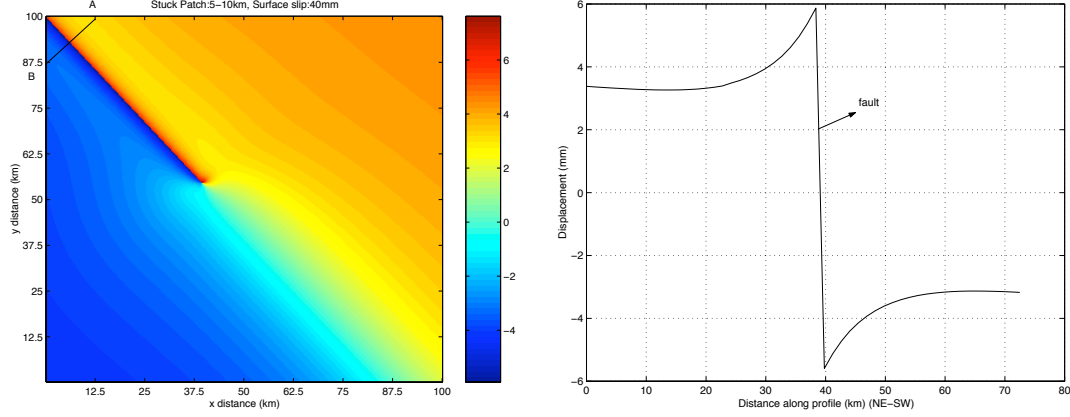
13

Figure 11: *Left*, Deformation along the radar line-of-sight for Model 3. *Right* Displacement profile along line AB

From the first scatterplot the displacement across the fault section is calculated to be 13 mm (or 3 radians). The second one has a 9 mm (or 2 rad) displacement. For 11 months interval, this displacement is a little high for the traditional value of 25 mm for the slip. The slip which gives this kind of a displacement is of the order of 30 mm to 40 mm per year.

We take phase profiles across Model 2 and the two different Model 3s, with a slip of 40 mm, from the same location of the fault as the first scatterplot. These four profiles are placed side by side in Figure 14. It is obvious from the shapes of the profiles that the scatter plot matches the Model 3 profiles more than the Model 2 profile, though it is not easy to decide which of the two models of 3 it resembles. Actually, even 40 mm slip rate gives a lesser displacement as compared to the first scatterplot. A higher value, say 45 mm, would be closer, but the second scatterplot has a displacement of 9 mm, so a conservative estimate for the creeping section slip is 40 mm.

4   Conclusion

The creeping section of the fault is clearly visible in not one but three differential interferograms. We believe that more interferograms with even better
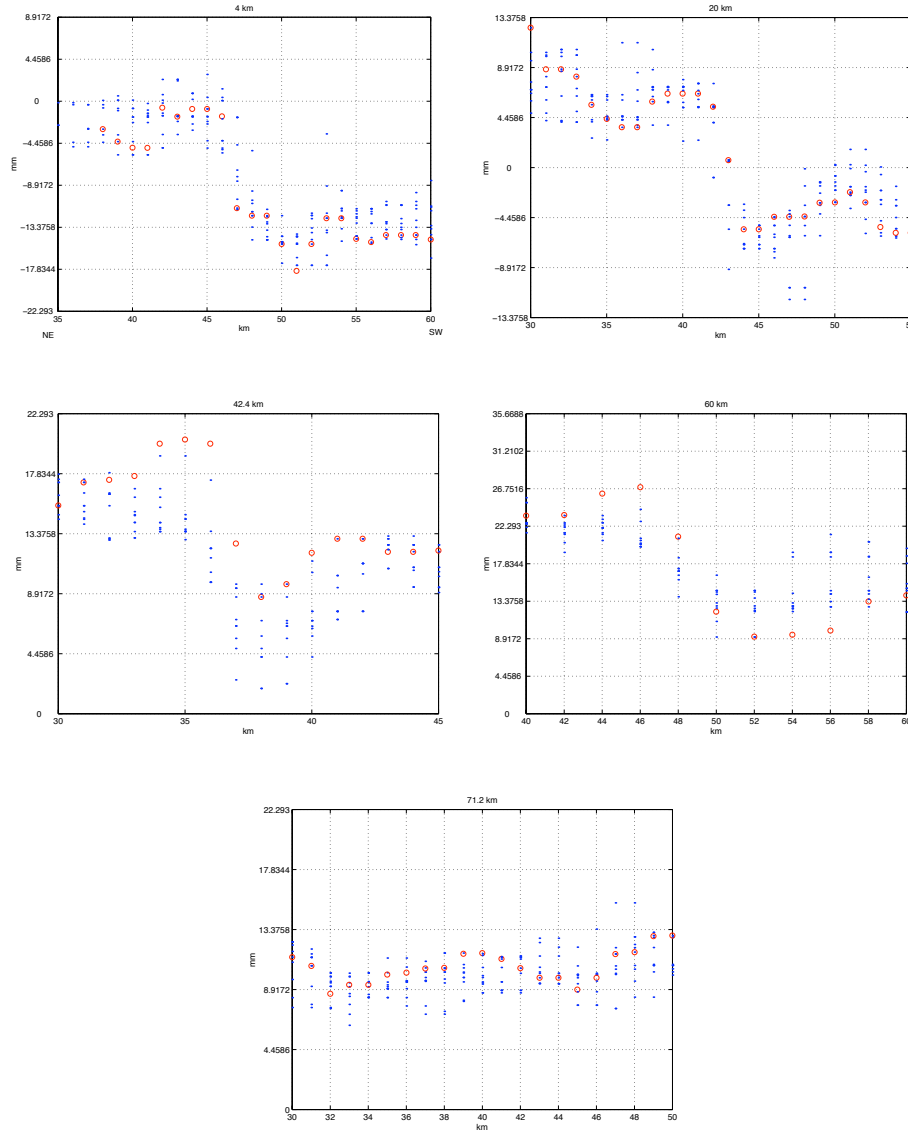
14

Figure 12: Phase scatterplots at 4 km, 20 km, 42.4 km, 60 km and 71.2 km from the NE corner
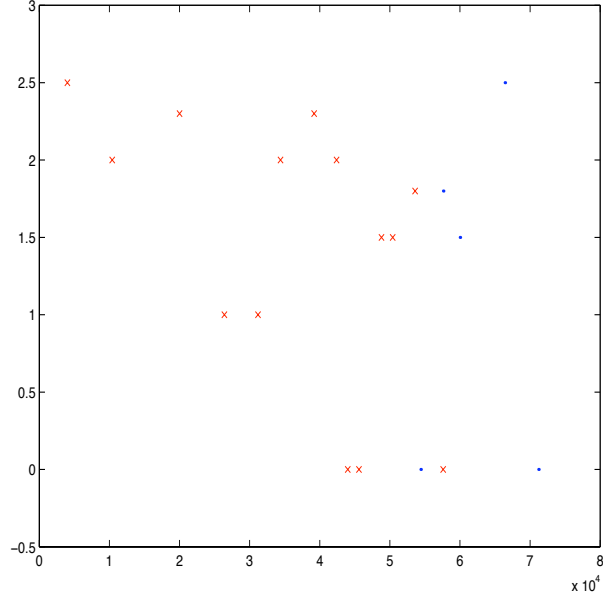
15

Figure 13: Phase difference along the fault

creep signature can be produced if we have an optimum set of images with a short perpendicular baseline, 10-15 months time interval and a clear atmosphere during measurments.

The 11 month interferogram predicts a higher slip rate (≈ 40 mm) at the creeping section. More interferograms are needed to understand this behaviour. It is probable that the fault was moving at a faster rate during that time. The average creep rate could be 25 mm but it is not neccessarily a constant value. From the modeling studies we can distinctly notice a difference in the deformation pattern between Model 2 and Model 3 i.e the linearly increasing slip rate and the 'stuck patch' model for the creeping section. Model 1 is not considered because of its unrealistic nature (the slip cannot change abruptly). It is difficult to see which of the two variations of Model 3 is closer to the data, since there is a lot of scatter in the data.

We can thus conclude from this study that it is possible to distinguish the fault behaviour if it is similar to either Model 2 or Model 3. For observing the deformation on the surface we need to have an unwrapped interferogram with very little decorrelation and atmospheric noise. It is evident that the far field
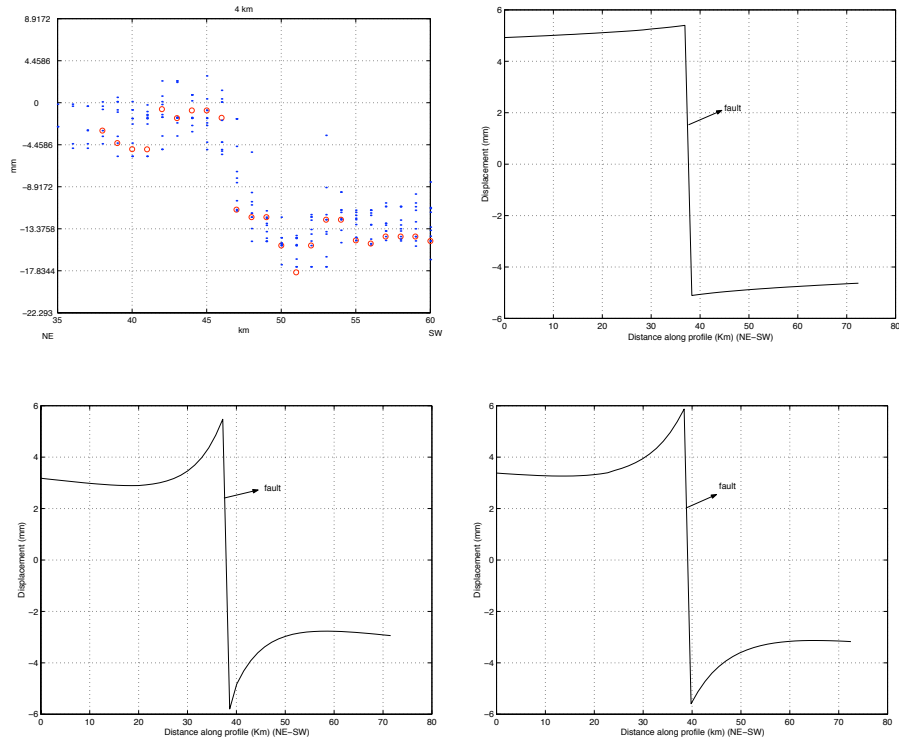
16

Figure 14: *Top Left*: Scatterplot from the interferogram 10130-5120, *Top Right*: Profile across fault in Model 2, *Bottom Left*: Profile across fault in Model 3 with 'stuck patch' at 3-8 km, *Bottom Right*: Profile across fault in Model 3 with 'stuck patch' at 5-10 km

pattern is same for both Models 2 and 3. It is only in the near field that we see the difference. This is very optimistic as the creep signal is better visible near the fault trace rather than far from the trace. Another important conclusion is the higher slip rate in the creeping section. This high value may be a one time effect or the fault creeps faster sometimes and slower the other times to give an average of 25 mm. A more comprehensive research integrated with other studies from this area, is required to determine the true behaviour of the fault.

5 References

Bakun, W. H. and Lindh, A.G.. The Parkfield, California earthquake prediction experiment, *Science*, 229, 1985

Goldstein, R. M., Engelhardt, H., Kamb,B., and Frolich, R. M. Satellite radar interferometry for monitoring ice sheet motion: Application to an Antarctic ice stream. *Science*, 262: 1525-1530, 1993

Harris, R., and Segall, P., Detection of a Locked Zone at Depth on the Parkfield, California Segment of the San Andreas Fault, *Journal of Geophysical Research*, Vol. 92, No. B8, pp 7945-7962, July,1987

Massonet, D., Briole, P., Arnaud, A., Deflation of Mount Etna monitored by spaceborn radar interferometry, *Nature*, 375, 567-570, 1995

Massonet, D., Rossi, M., Carmona, C., Adragna, F., Peltzer, G., Feigl, K., and Rabaute, T., The displacement field of the Lander's earthquake, *Nature*, 364, 138-142, 1993

Okada, Y., Surface Deforamtion due to Shear and Tensile Faults in a Half-Space, *Bulletin of the Seismological Society of America*, Vol. 75, No. 4, pp1135-1154, August 1985

Prati, C., Rocca, F., Ferreti, A., An overview of SAR interferometry, *http://earth.esa.int/florence/p details/speeches/rocca-et-al/*, 2000

Rodriguez, E., Martin, J. M., Theory and design of interferometric synthetic aperture radars, *IEEE Proceedings-F*, Vol.139, No.2, 147-159, 1992

Rosen, P., Werner, C. L., Hensley, S., Fielding, E., Buckley., S., and Vincent, P., Aseismic creep along the San Andreas Fault northwest of Parkfield, California measured by radar interferometry, *Geophysical Research Letters*, Vol. 25, No. 6, 825-828, 1998

Zebker, H. A. and Goldstein, R., Topographic mapping from interferometric SAR observations, *Journal of Geophysical Research*, 91, 4993-5001, 1986